JOURNAL OF SPACECRAFT AND ROCKETS
Vol. 45, No. 5, September–October 2008

Radiative Heat Transfer Analysis with Molten Al_2O_3 Dispersion in Solid Rocket Motors

Jy-Yun Jung* and M. Q. Brewster†
University of Illinois at Urbana–Champaign, Urbana, Illinois 61801

DOI: 10.2514/1.30018

Radiative heat transfer by alumina smoke particles (molten Al_2O_3) in aluminized solid rocket motor internal flowfields has been investigated by computational simulation. The issue of how to define the alumina dispersion's radiative properties has been addressed to be compatible with existing radiative transfer equation solvers. Individual particle radiative properties, which are nongray and anisotropic in scattering, are evaluated from fundamental particle scattering theory for spheres (i.e., Mie theory) and optical constants from the literature, including temperature and spectral dependence. An integration procedure over wavelength has been implemented to make use of the effective gray form of two common radiative transfer equation solvers: the finite volume method and Rosseland diffusion radiation model. The internal flowfield has been modeled including turbulent multiphase flow with inert radiating particles using commercial computational fluid dynamics software. The simulation has been exercised for a subscale solid rocket motor, the 75-lb ballistic test and evaluation systems motor. Simulation results show that the bulk of the internal flowfield (the core flow) is very optically thick, so much so as to be amenable to Rosseland diffusion modeling.

Nomenclature

A	=	projected area
a	=	absorption coefficient
D	=	particle diameter, μm
$f(\lambda T)$	=	blackbody fractional function
f_{pn}	=	particle-scattering factor
I	=	intensity
$K_{eI,R}$	=	Rosseland extinction coefficient
k	=	absorption index
N	=	particle number density
n	=	refractive index
Q_a	=	absorption efficiency
Q_e	=	extinction efficiency
Q_s	=	scattering efficiency
r	=	particle radius
$\mathbf{r}$	=	position vector
$\mathbf{s}$	=	direction vector
$\mathbf{s}'$	=	scattering direction vector
T	=	particle temperature
T_e	=	blackbody irradiation temperature
V	=	volume
γ_{pn}	=	particle extinction efficiency (Rosseland mean)
ε_{pn}	=	particle emissivity
θ	=	single-scattering particle polar angle
ρ_{pn}	=	particle reflectivity
σ_p	=	particle-scattering coefficient
σ	=	Stefan–Boltzmann constant (5.672×10^{-8} W/m^{2}K^4)
Φ	=	phase function
Ω'	=	solid angle
ω_0	=	single-scattering albedo

Subscripts

a	=	absorption
b	=	blackbody
e	=	extinction
I	=	isotropic
n	=	particle number
p	=	particle
s	=	scattering
λ	=	wavelength

Superscripts

*	=	nondimensional

Received 27 March 2007; revision received 12 February 2008; accepted for publication 13 February 2008.

*Graduate Student, Department of Mechanical Science and Engineering; jung1@uiuc.edu.
†Hermia G. Soo Professor, Department of Mechanical Science and Engineering; brewster@uiuc.edu. Fellow AIAA.

I. Introduction

FOR multiphase reacting flows, it is often desirable to include radiation effects in the flow solver due to the presence of condensed-phase species and their continuum emission/absorption. One important example is an aluminized solid rocket motor (SRM), which contains micron-sized molten Al_2O_3 particles as a combustion product. It has been shown that radiative heat transfer is important in aluminized solid rocket motors, both to the propellant surface [1–5] and to other internal surfaces [6]. Hence, it is reasonable to include the radiation effect to the simulation of aluminized SRMs. Accordingly, although there have been a couple of other ways to solve the radiative transfer equation (RTE), radiation also has been attempted to be simulated with the finite volume method (FVM) so that it can be solved based on the same philosophy and computational grid as the fluid flow solver [7,8]. Murthy and Mathur [9] extended this FVM for radiation to unstructured meshes and, in doing so, built the foundation for the discrete ordinate model in FLUENT. This method works across all ranges of optical thickness and can be conveniently applied to arbitrary geometry; however, convergence becomes slower as optical thickness increases.

In spite of this development, radiation is not always incorporated into the internal flow simulation in a solid rocket motor with a metallized propellant [10,11]. One reason is the dramatic CPU time increase by inclusion of the radiation, especially when an exact intensity field is intended. This is because particles from the metal combustion are nongray (although not as much as molecular gases) and strongly anisotropic in-scattering, which requires high resolutions in spectral and angular discretization.

The objective of the present work is to simulate and investigate the internal flowfield in an aluminized SRM including nongray particle radiation and, in particular, to define radiative properties of an assembly of molten Al_2O_3 particles for internal SRM flows in a

format recognized by the effective gray form of RTE solvers: the discrete-ordinates model as interpreted in a FVM manner and the Rosseland approximation. These effective gray properties are derived from the fundamental particle properties of size and optical constants (n, k). An integration procedure over wavelength and particle size is implemented. There are two essential tasks in this process: the first is to define the volumetric radiative properties of an assembly of alumina particles in an optically thin, single-scattering control volume of arbitrary number density based on the fundamental individual particle properties, and the second is to implement a discrete-phase model to determine local particle number densities and hence local volumetric radiative properties and thereby the radiation field. Proceeding in this way allows separate and external evaluation of the flow-independent radiative properties, which can be used as needed in the computational fluid dynamics (CFD) analysis of the spatially nonhomogeneous internal flowfield. Illustrative calculations are presented for nonreacting particles (i.e., inert Al_2O_3 particles, not burning Al/Al_2O_3 droplets) in a 75 lb BATES (Ballistic Test and Evaluation Systems) motor [12].

II. Finite Volume Method

In this work it is assumed that radiation by gases is negligible compared with that by particles. Solid-propellant burning-rate studies have shown that radiative heat feedback in metallized propellants is much more likely to be significant compared with conductive heat feedback than in nonmetallized propellants [1–3]. With respect to heat transfer to nonpropellant internal surfaces (such as internal insulators), in a theoretical study, Duval et al. [6] showed that the radiative heat flux dominated by particle radiation. Based on equilibrium calculations at 3400 K and 50 MPa, the important radiating species were CO_2, CO, H_2O, HCl, and Al_2O_3.

The radiative properties of alumina particles (molten Al_2O_3) are dependent on wavelength. To evaluate total or effective gray radiative properties, we start from the spectral RTE:

$$\nabla \cdot (I_\lambda \mathbf{s}) + (a_{p\lambda} + \sigma_{p\lambda}) I_\lambda(\mathbf{r}, \mathbf{s}) = a_{p\lambda} I_{b\lambda} + \frac{\sigma_{p\lambda}}{4\pi} \int_0^{4\pi} I_\lambda(\mathbf{r}, \mathbf{s}') \Phi_\lambda(\mathbf{s} \cdot \mathbf{s}') \, \mathrm{d}\Omega' \tag{1}$$

where participation by gas has been ignored. The term $(a_{p\lambda} + \sigma_{p\lambda}) I_\lambda(\mathbf{r}, \mathbf{s})$ represents volumetric absorption and out-scattering by particles, which is extinction of radiation in a control volume; this is a sink term, causing a decrease of intensity along a line of sight. The terms $a_{p\lambda} I_{b\lambda}$ and

$$\frac{\sigma_{p\lambda}}{4\pi} \int_0^{4\pi} I_\lambda(\mathbf{r}, \mathbf{s}) \Phi_\lambda(\mathbf{s} \cdot \mathbf{s}') \, \mathrm{d}\Omega'$$

represent blackbody emission and in-scattering by particles, respectively; these are volumetric source terms, meaning they give rise to an increase of intensity along a line of sight.

The following sections discuss how to integrate the spectral RTE term by term to get total or effective gray radiative properties of particles for the absorption, emission, in-scattering, and out-scattering terms. A distribution of particles sizes has been considered in the form of a discrete distribution. The dispersion's radiative properties are assumed to be the sum of all particles' individual properties; that is, the particles are assumed to interact with the radiation incident upon them as if uninfluenced by the presence of neighboring particles (i.e., the independent scattering assumption) [13].

A. Emission Term

The particle emission term is integrated over the wavelength as follows:

$$\int_0^\infty a_{p\lambda} I_{b\lambda} \, \mathrm{d}\lambda = I_b(T) \int_0^\infty a_{p\lambda}(T) \frac{I_{b\lambda}(T)}{I_b(T)} \, \mathrm{d}\lambda = I_b(T) \int_0^1 a_{p\lambda}(T) \, \mathrm{d}f(\lambda T) \tag{2}$$

where T is the particle temperature. Next, the size distribution is included. Because the scattering and absorption properties of a particle of a given size depend on the incident intensity's wavelength, we start with the following spectral form:

$$a_{p\lambda}(T) = \int_0^\infty \pi r^2 Q_a(r, T) N(r) \, \mathrm{d}r \tag{3}$$

where r is the radius of a particle, and N is the number of particles in a control volume. The term $Q_a(r, T)$ is the absorption efficiency and is a spectral property. Therefore, the effective gray particle emission with size distribution using Eq. (2) would be

$$\begin{aligned} I_b(T) \int_0^1 a_{p\lambda}(T) \, \mathrm{d}f(\lambda T) &= I_b(T) \int_0^1 \int_0^\infty \pi r^2 Q_a(r, T) N(r) \, \mathrm{d}r \, \mathrm{d}f(\lambda T) \\ &= I_b(T) \int_0^\infty \pi r^2 N(r) \left[\int_0^1 Q_a(r, T) \, \mathrm{d}f(\lambda T) \right] \mathrm{d}r \\ &= \sum_{r_n} \pi r_n^2 N(r_n) I_b(T) \int_0^1 Q_a(r_n, T) \, \mathrm{d}f(\lambda T) \end{aligned} \tag{4}$$

$$\Leftrightarrow \lim_{V \to 0} \sum_{n=1}^{N} \frac{A_{pn}}{V} \frac{\sigma T_{pn}^4}{\pi} \varepsilon_{pn} \tag{5}$$

Equation (4) is our suggested integration over wavelength and size for the particle's emission in a polydisperse particle assembly based on fundamental radiative property definitions. Equation (5) is quoted from [14] and shows how the gray RTE solver defines the particle's emission in a control volume. The parameter ε_{pn} is called particle emissivity. Noting the correspondence between

$$\sum_{r_n} \pi r_n^2 N(r_n)$$

and

$$\lim_{V \to 0} \sum_{n=1}^{N} \frac{A_{pn}}{V}$$

the following definition of particle emissivity is deduced:

$$\varepsilon_{\mathrm{pn}} \Leftrightarrow \int_0^1 Q_a(r_n, T) \, \mathrm{d}f(\lambda T) \tag{6}$$

Note that this particle emissivity is not the fundamental definition of emissivity but is defined to make use of a gray radiation solver and fundamental particle radiative properties.

B. Absorption Term

The particle absorption term is

$$\int_0^\infty a_{p\lambda} I_\lambda \, \mathrm{d}\lambda$$

where I_λ is the local intensity incident on a control volume. To evaluate this term, for property definition purposes, the assumption is made that the local intensity or irradiation is proportional to blackbody radiation at an environment temperature T_e:

$$\int_0^\infty a_{p\lambda} I_\lambda \, \mathrm{d}\lambda = I_b(T_e) \int_0^\infty a_{p\lambda}(T) \frac{I_{b\lambda}(T_e)}{I_b(T_e)} \, \mathrm{d}\lambda = I_b(T_e) \int_0^1 a_{p\lambda}(T) \, \mathrm{d}f(\lambda T_e) \tag{7}$$

This assumption is most appropriate in optically thick regions of the flow. In optically thin regions, however, the possibility exists that the real irradiation is different, with intensity coming from both distant colder regions and distant hotter regions. These variations tend to be

averaged out, even in optically thin regions, thus justifying the approximation. Furthermore, the blackbody irradiation assumption is only used for defining the total radiative properties, not for describing the discrete ordinate intensities in the RTE. A further additional assumption used here (but only for illustrative purposes) is that the local environment temperature and local particle temperature are the same, $T_e = T$.

The absorption term's spectral integration is done in the same manner as the emission term. The integral term

$$\int_0^1 a_{p\lambda}(T)\,\mathrm{d}f(\lambda T_e)$$

corresponds to the total absorption coefficient, which will be used as the effective gray property a_p in the FVM for the gray RTE solver:

$$a_p = \int_0^1 a_{p\lambda}(T)\,\mathrm{d}f(\lambda T_e) \tag{8}$$

After introducing size distribution such as in Eq. (4), the effective gray absorption coefficient would be

$$\begin{aligned} a_p &= \int_0^1 \int_0^\infty \pi r^2 Q_a(r,T) N(r)\,\mathrm{d}r\,\mathrm{d}f(\lambda T_e) \\ &= \int_0^\infty \pi r^2 N(r) \left[\int_0^1 Q_a(r,T)\,\mathrm{d}f(\lambda T_e) \right] \mathrm{d}r \\ &= \sum_{r_n} \pi r_n^2 N(r_n) \int_0^1 Q_a(r_n,T)\,\mathrm{d}f(\lambda T_e) \end{aligned} \tag{9}$$

$$\Leftrightarrow \lim_{V\to 0} \sum_{n=1}^{N} \frac{A_{pn}}{V} \alpha_{pn} \tag{10}$$

Equation (9) is our suggested integration over wavelength and size for the total absorption coefficient in a polydisperse particle assembly based on fundamental radiative property definitions. Equation (10) is quoted from [14], except that α_{pn} is used instead of ε_{pn}. This shows how the gray RTE solver defines the absorption coefficient in a control volume. Noting the correspondence between

$$\sum_{r_n} \pi r_n^2 N(r_n)$$

and

$$\lim_{V\to 0} \sum_{n=1}^{N} \frac{A_{pn}}{V}$$

the following definition of particle absorptivity is deduced:

$$\alpha_{pn} \Leftrightarrow \int_0^1 Q_a(r_n,T)\,\mathrm{d}f(\lambda T_e) \tag{11}$$

The parameter α_{pn} is considered to be the same as particle emissivity ε_{pn} in [14]. Technically, however, it is particle absorptivity, because the environment temperature is used to characterize the blackbody radiation instead of the particle temperature (if they are different). As noted, because the two temperatures are assumed to be the same in this work, the particle emissivity and absorptivity are the same, effectively.

Next, we consider a useful decomposition that can be applied to all the total volumetric radiative properties. The volumetric absorption (or emission) coefficients for an assembly of particles defined in Eqs. (4) and (9) are composed of two parts: a part describing individual particle's absorptivity/emissivity $\alpha_{pn}/\varepsilon_{pn}$ and a part dependent on particle size and number density:

$$\sum_{r_n} \pi r_n^2 N(r_n)$$

The first part, the individual particle's effective gray absorptivity/emissivity, is a function of its size and optical constants and can be evaluated from Mie theory. The second part factors in the number of particles in a small volume; this is the part that is dependent on the flow. Thus, the nonhomogeneous dispersion's volumetric radiative properties (emission, absorption, and scattering) may all be separated into two parts that can be calculated from Mie scattering theory and a discrete-phase CFD model. This feature insures that the former (Mie scattering calculation) can be done externally and provided to the CFD code. This reduces the radiative contribution to the computation in the internal flow solver.

C. Out-Scattering Term

The procedure for scattering is similar to that for absorption. Just the two integrands need to be changed from absorption to scattering:

$$a_{p\lambda} \Rightarrow \sigma_{p\lambda}, \qquad Q_a \Rightarrow Q_s \tag{12}$$

Then the out-scattering term in the spectral RTE becomes

$$\begin{aligned} \int_0^\infty \sigma_{p\lambda} I_\lambda\,\mathrm{d}\lambda &= I_b(T_e) \int_0^\infty \sigma_{p\lambda}(T) \frac{I_{b\lambda}(T_e)}{I_b(T_e)}\,\mathrm{d}\lambda \\ &= I_b(T_e) \int_0^1 \sigma_{p\lambda}(T)\,\mathrm{d}f(\lambda T_e) \end{aligned} \tag{13}$$

Therefore, the effective gray scattering coefficient is

$$\begin{aligned} \sigma_p &= \int_0^1 \sigma_{p\lambda}(T)\,\mathrm{d}f(\lambda T_e) \\ &= \int_0^1 \int_0^\infty \pi r^2 Q_s(r,T) N(r)\,\mathrm{d}r\,\mathrm{d}f(\lambda T_e) \\ &= \int_0^\infty \pi r^2 N(r) \left[\int_0^1 Q_s(r,T)\,\mathrm{d}f(\lambda T_e) \right] \mathrm{d}r \\ &= \sum_{r_n} \pi r_n^2 N(r_n) \int_0^1 Q_s(r_n,T)\,\mathrm{d}f(\lambda T_e) \end{aligned} \tag{14}$$

$$\Leftrightarrow \lim_{V\to 0} \sum_{n=1}^{N} \frac{A_{pn}}{V} (1 - f_{pn})(1 - \varepsilon_{pn}) \tag{15}$$

Equation (14) is our suggested integration over wavelength and size for the total scattering coefficient in multiple-sized particles' assembly based on fundamental radiative property definitions. Equation (15) is how the gray RTE solver defines the total scattering coefficient in a control volume. Therefore, the following is deduced:

$$(1 - f_{pn})(1 - \varepsilon_{pn}) \Leftrightarrow \int_0^1 Q_s(r_n,T)\,\mathrm{d}f(\lambda T_e) \tag{16}$$

where f_{pn} is called the particle-scattering factor. The particle-scattering factor, in terms of fundamental properties, is

$$f_{pn} = \frac{1 - \int_0^1 Q_e(r_n,T)\,\mathrm{d}f(\lambda T_e)}{1 - \int_0^1 Q_a(r_n,T)\,\mathrm{d}f(\lambda T)} \tag{17}$$

The interpretation of f_{pn} is not necessarily obvious, however. Historically, its definition seems based on coal-particle radiation analysis [15]. It is a measure of deviation from the extinction efficiency of 1. For particles much larger than the wavelength (such as coal and char particles), the extinction efficiency approaches 1 if the diffraction contribution to scattering (which is highly forward-anisotropic) is neglected. This is the so-called geometric optics regime. In this regime ($Q_e = 1$), the particle-scattering factor is zero, as the numerator of Eq. (17) shows. If diffraction is included, Q_e approaches 2 and Q_a approaches a positive constant less than 1; then f_{pn} is negative. As particle size is reduced to the order of wavelength, it becomes necessary to include full-anisotropic scattering (Mie scattering), and the extinction efficiency is a complicated function of size and wavelength due to wave interference. As particle size is reduced further to the regime in which it is much smaller than the wavelength, the so-called Rayleigh scattering regime, the extinction

efficiency becomes less than unity. In this regime, f_{pn} is positive, because Q_a is always less than Q_e. The f_{pn} factor serves as a normalizing factor, allowing the term $1-\varepsilon_{pn}$ to be used in Eq. (15) to evaluate a particle's reflection/scattering strength relative to its total extinction (absorption plus scattering) strength even when the total extinction cross section is different from the geometric cross section; that is, when $\varepsilon_{pn}+\rho_{pn}\neq 1$, where ρ_{pn}, the total particle-scattering efficiency or reflectivity, is defined by a modified form of Eq. (18):

$$\begin{gathered}\sigma_p - \lim_{V\to 0}\sum_{n=1}^{N}\frac{A_{pn}}{V}\rho_{pn} \\ \rho_{pn} \Leftrightarrow \int_0^1 Q_s(r_n,T)\,\mathrm{d}f(\lambda T_e) \Leftrightarrow (1-f_{pn})(1-\varepsilon_{pn})\end{gathered} \tag{18}$$

For example, for small particles (Rayleigh scatterers), the particle emissivity/absorptivity and reflectivity add to a positive number less than 1 and f_{pn} is a positive number less than 1, as defined by a modified form of Eq. (19):

$$f_{pn} = \frac{1-(\varepsilon_{pn}+\rho_{pn})}{1-\varepsilon_{pn}} \tag{19}$$

D. In-Scattering Term

The in-scattering term in the spectral RTE is

$$\frac{\sigma_{p\lambda}}{4\pi}\int_0^{4\pi} I_\lambda(\mathbf{r},\mathbf{s}')\Phi_\lambda(\mathbf{s}\cdot\mathbf{s}')\,\mathrm{d}\Omega' \tag{20}$$

The spectral-directional scattered energy is

$$\sigma_{p\lambda} I_\lambda(\mathbf{r},\mathbf{s}')\Phi_\lambda(\mathbf{s}\cdot\mathbf{s}') \tag{21}$$

By integrating over wavelength and assuming blackbody irradiation, the total-directional scattered energy becomes

$$\begin{gathered}I_b(T_e)\int_0^\infty \sigma_{p\lambda}\Phi_\lambda(\mathbf{s}\cdot\mathbf{s}')\frac{I_{b\lambda}(T_e)}{I_b(T_e)}\,\mathrm{d}\lambda \\ I_b(T_e)\int_0^1 \sigma_{p\lambda}\Phi_\lambda(\mathbf{s}\cdot\mathbf{s}')\,\mathrm{d}\lambda(\lambda T_e)\end{gathered} \tag{22}$$

Introducing a size distribution function for an assembly of particles $N(r)$, the scattering coefficient $\sigma_{p\lambda}$ and phase function Φ_λ for an assembly or dispersion of particles can be written as in [16]:

$$\begin{aligned}\sigma_{p\lambda} &= \int_0^\infty \pi r^2 Q_s(r)N(r)\,\mathrm{d}r \\ \Phi_\lambda &= \frac{\int_0^\infty \pi r^2 Q_s(r)\Phi_\lambda(r)N(r)\,\mathrm{d}r}{\int_0^\infty \pi r^2 Q_s(r)N(r)\,\mathrm{d}r} \\ \sigma_{p\lambda}\Phi_\lambda &= \int_0^\infty \pi r^2 N(r)Q_s(r)\Phi_\lambda(r)\,\mathrm{d}r\end{aligned} \tag{23}$$

Therefore, the total-directional scattered energy becomes

$$\begin{aligned}&I_b(T_e)\int_0^1 \sigma_{p\lambda}\Phi_\lambda\,\mathrm{d}f(\lambda T_e) \\ &\quad= I_b(T_e)\int_0^\infty \pi r^2 N(r)\int_0^1 Q_s(r)\Phi_\lambda(r)\,\mathrm{d}f(\lambda T_e)\,\mathrm{d}r \\ &\quad= I_b(T_e)\sum_{r_n}\pi r_n^2 N(r_n)\int_0^1 Q_s(r_n,T)\Phi_\lambda(r_n,T)\,\mathrm{d}f(\lambda T_e)\end{aligned} \tag{24}$$

With this result, the effective gray form of the in-scattering term [Eq. (13)] becomes

$$\frac{I_b(T_e)}{4\pi}\int_0^{4\pi}\sum_{r_n}\pi r_n^2 N(r_n)\int_0^1 Q_s(r_n,T)\Phi_\lambda(r_n,T)\,\mathrm{d}f(\lambda T_e)\,\mathrm{d}\Omega' \tag{25}$$

The in-scattering term in the gray RTE is

$$\frac{\sigma_p}{4\pi}\int_0^{4\pi} I(\mathbf{r},\mathbf{s}')\Phi(\mathbf{s}\cdot\mathbf{s}')\,\mathrm{d}\Omega'$$

By comparing this with Eq. (20), it is deduced that

$$\sigma_p\Phi(\mathbf{s}\cdot\mathbf{s}') \Leftrightarrow \sum_{r_n}\pi r_n^2 N(r_n)\int_0^1 Q_s(r_n,T)\Phi_\lambda(r_n,T)\,\mathrm{d}f(\lambda T_e) \tag{26}$$

Therefore, the effective gray phase function has the correspondence shown next:

$$\begin{aligned}\Phi(\mathbf{s}\cdot\mathbf{s}') &\Leftrightarrow \frac{\sum_{r_n}\pi r_n^2 N(r_n)\int_0^1 Q_s(r_n,T)\Phi_\lambda(r_n,T)\,\mathrm{d}f(\lambda T_e)}{\sum_{r_n}\pi r_n^2 N(r_n)\int_0^1 Q_s(r_n,T)\,\mathrm{d}f(\lambda T_e)} \\ &= \frac{\int_0^1 \sigma_{p\lambda}\Phi_\lambda\,\mathrm{d}f(\lambda T_e)}{\sigma_p}\end{aligned} \tag{27}$$

This is how the effective gray scattering phase function $\Phi(\mathbf{s}\cdot\mathbf{s}')$ in the gray RTE is defined.

To summarize, particle emissivity, particle-scattering factor, and phase function (input parameters in the gray RTE) have been defined in Eqs. (6), (17), and (27), respectively. To perform these equations' integration, the spectral absorption and scattering efficiencies, spectral phase function, and number densities have to be known. The first three terms need to be calculated with the Mie scattering theory, whereas the number densities can be retrieved from a discrete-phase model.

E. Evaluation of Particle Emissivity and Scattering Factor

The definitions of particle emissivity and scattering factor from Eqs. (6) and (17) are

$$\begin{aligned}\varepsilon_{pn} &\Leftrightarrow \int_0^1 Q_a(r,T,\lambda)\,\mathrm{d}f(\lambda T) \\ f_{pn} &\Leftrightarrow \frac{1-\int_0^1 Q_e(r,T,\lambda)\,\mathrm{d}f(\lambda T_e)}{1-\int_0^1 Q_a(r,T,\lambda)\,\mathrm{d}f(\lambda T_e)}\end{aligned}$$

where

$$Q_a(r,T,\lambda) = Q_e(r,T,\lambda) - Q_s(r,T,\lambda)$$

Wavelength λ has been noted as a variable for clarification. The extinction and scattering efficiencies Q_e and Q_s have been calculated from Mie scattering theory. The optical constants $n-ik$ have been retrieved from Parry and Brewster [17]. They obtained temperature-dependent optical constants of molten Al_2O_3 smoke particles between 0.5 and 5.0 μm and temperatures between 2320 and 3000 K by carrying out a dispersion analysis on selected data from other investigations [18,19]. To show an example calculation, we used the discretized values of optical constant at 6 wavelengths (0.5, 1.0, 2.0, 3.0, 4.0, and 5.0 μm) and 5 temperatures (2300, 2500, 2700, 2800, and 3000 K).

In Fig. 1, the solid line is $Q_e(r,T,\lambda)$, and the dotted one is $Q_s(r,T,\lambda)$ for $D=1.2$ μm Al_2O_3 smoke particles at 3000 K. It illustrates both the large (geometric optics plus diffraction) particle-scattering regime and the small (Rayleigh) particle-scattering regime. In the former (smaller wavelengths), Q_e tends toward 2 (because diffraction has been included), and in the latter (larger wavelengths), it decreases below 1.

Figures 2 and 3 show the spectral integration of $Q_a(r,T,\lambda)$ and $Q_e(r,T,\lambda)$ as part of the process for obtaining ε_{pn} and f_{pn}; in fact, Fig. 2 is the particle emissivity/absorptivity. In Fig. 2, the higher values of ε_{pn} for bigger particles might seem to imply that bigger particles are more important in terms of emission and absorption; in fact, they are not as important radiatively in the solid rocket motor model as the 1.2 μm particles because of their low number densities.

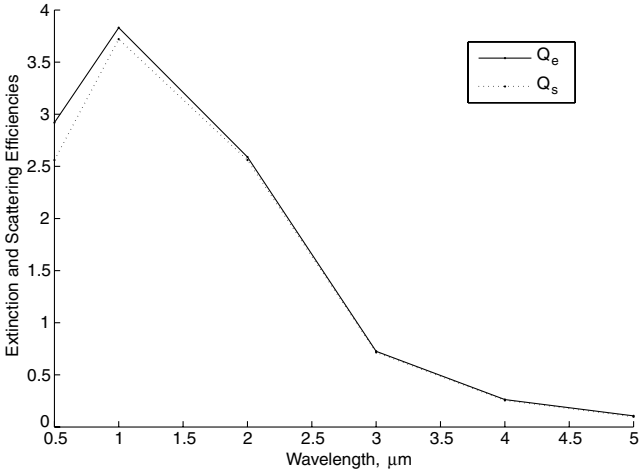

Fig. 1 Extinction and scattering efficiencies $Q_e(r, T, \lambda)$ and $Q_s(r, T, \lambda)$ for alumina particles for size $D = 1.2$ μm at 3000 K.

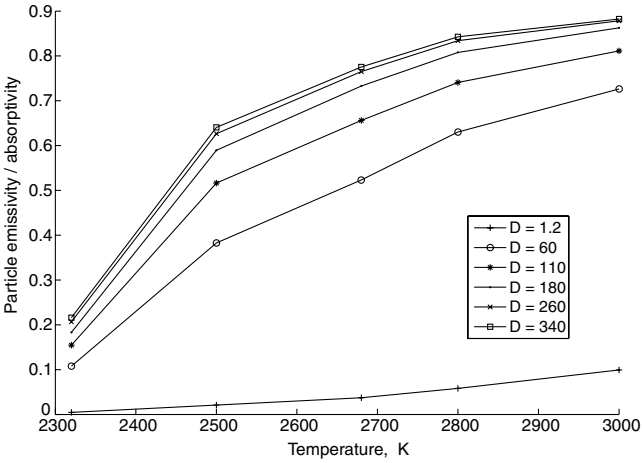

Fig. 2 Particle emissivity/absorptivity $\varepsilon_{pn} = \int_0^1 Q_a(r, T, \lambda)\, \mathrm{d}f(\lambda T)$ at different sizes and temperatures.

In terms of emission and absorption characteristics, it is important to remember that Figs. 2 and 3 only indicate the behavior of individual particles. The volumetric properties (e.g., emissivity) of an assembly or distribution of particles depend on the local particles' number densities. Figure 2 indicates that the 1.2 μm particles are individually weak emitters compared with the bigger particles. However, these particles' low ε_{pn} is compensated for by their high

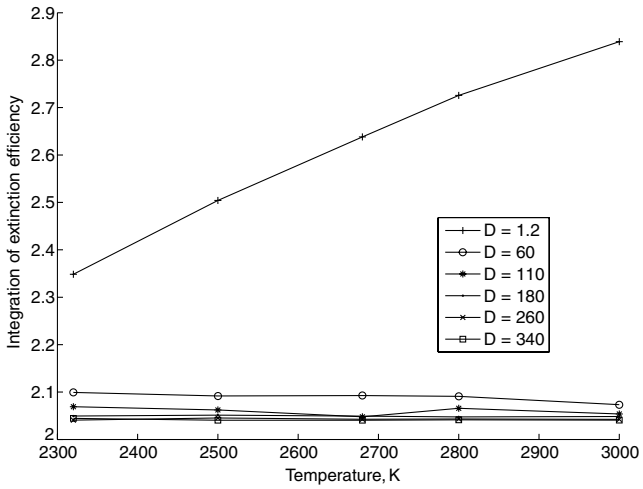

Fig. 3 Integration of extinction efficiency $\int_0^1 Q_e(r, T, \lambda)\, \mathrm{d}f(\lambda T_e)$ at different sizes and temperatures.

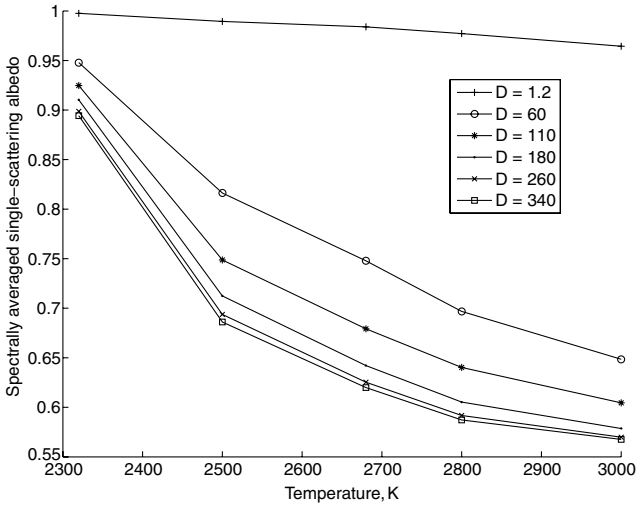

Fig. 4 Spectrally averaged single-scattering albedo ω_0^* at different sizes and temperatures.

number density in the motor flow environment (discussed next) and, as a result, they dominate emission by the assembly.

Figure 4 shows the ratio of scattering to extinction (scattering plus absorption), which is often referred to as single-scattering albedo ω_0. Strictly speaking, the albedo is a spectral property. Here, in order to get a general idea of particle behavior, a spectrally integrated ratio

$$\omega_0^* = \frac{\int_0^1 Q_s(r, T, \lambda)\, \mathrm{d}f(\lambda T_e)}{\int_0^1 Q_e(r, T, \lambda)\, \mathrm{d}f(\lambda T_e)}$$

has been defined and evaluated (Fig. 4). It can be deduced that the radiative behavior in the SRM is dominated by 1.2 μm particles, having a very strong scattering contribution, because of their high albedo value and number density.

Figure 5 shows the results for f_{pn}. As can be seen in Fig. 5, and as already discussed according to Eq. (17), f_{pn} is negative because

$$\int_0^1 Q_e\, \mathrm{d}f$$

approaches 2 (diffraction has not been excluded) and

$$\int_0^1 Q_a\, \mathrm{d}f$$

approaches a positive constant less than 1.

As an alternative parameter to f_{pn}, the particle reflectivity or scattering efficiency ρ_{pn} defined in Eq. (18) can be evaluated. Figure 6 shows that the particle reflectivity values are generally

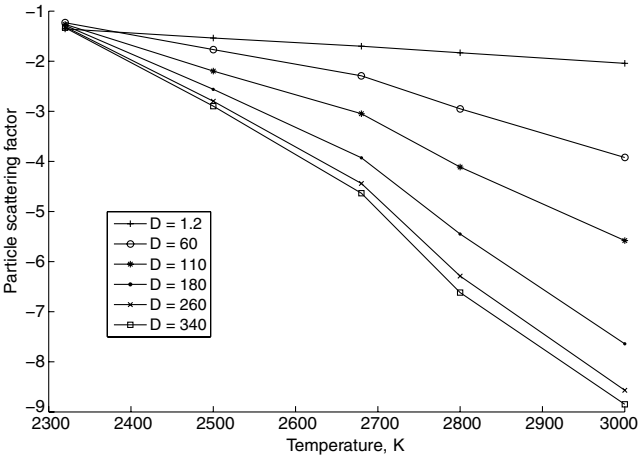

Fig. 5 Particle-scattering factor at different sizes and temperatures.

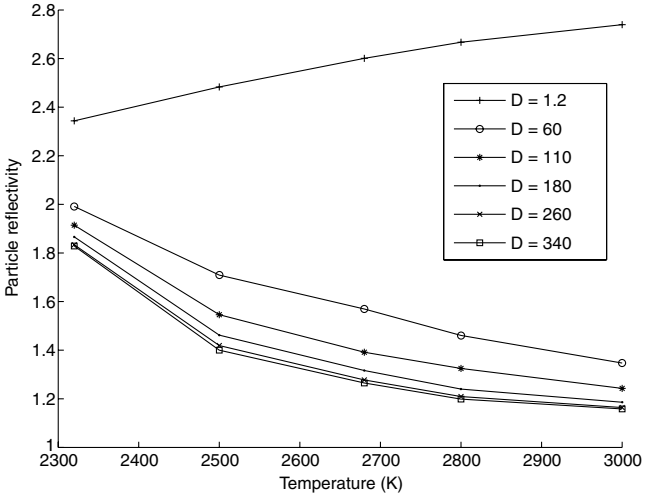

Fig. 6 Particle reflectivity (scattering efficiency) $\rho_{pn} \Leftrightarrow \int_0^1 Q_s(r, T, \lambda)\, \mathrm{d}f(\lambda T_e)$ at different sizes and temperatures.

greater than the corresponding emissivity values (Fig. 2), and particularly so for the important 1.2 μm particles (this fact was also indicated in the albedo values of Fig. 4). Furthermore, the reflectivity values are greater than 1, indicating that the effective scattering cross sections are greater than the geometric cross sections, which is a consequence of the size of the particles being of the order of, or slightly larger than, the wavelength.

F. Evaluation of Phase Function

The effective gray phase function of particle dispersion is defined in Eq. (27):

$$\Phi(\mathbf{s}\cdot\mathbf{s}') = \frac{\sum_{r_n} \pi r_n^2 N(r_n) \int_0^1 Q_s(r_n, T, \lambda)\Phi_\lambda(r_n, T, \lambda, \theta)\, \mathrm{d}f(\lambda T_e)}{\sum_{r_n} \pi r_n^2 N(r_n) \int_0^1 Q_s(r_n, T, \lambda)\, \mathrm{d}f(\lambda T_e)}$$

For clarification, all independent variables are noted inside of the parentheses. Here, θ is the single-scattering particle polar angle (the angle between the incoming and outgoing directions). Depending on a particle's size, the particle's phase function showed a very distinctive behavior. Figures 7 and 8 show the spectral phase functions of 1.2 and 60 μm particles, respectively.

Figure 8 shows that when a particle's size is big enough, there is a strong forward-scattering and, effectively, almost no scattering. Therefore, in order to express this analytically, it is prudent to use a Delta–Eddington approximation [16], in which the forward-scattering peak is separated from the rest of the scattering phase function by

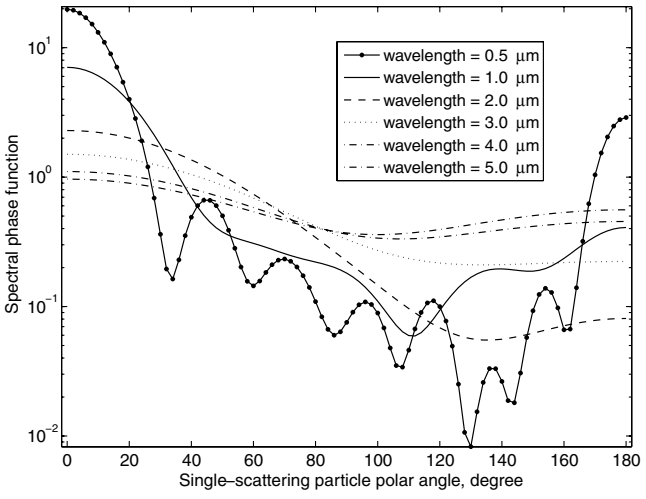

Fig. 7 Log scale spectral phase function of $D = 1.2$ μm at $T = 3000$ K.

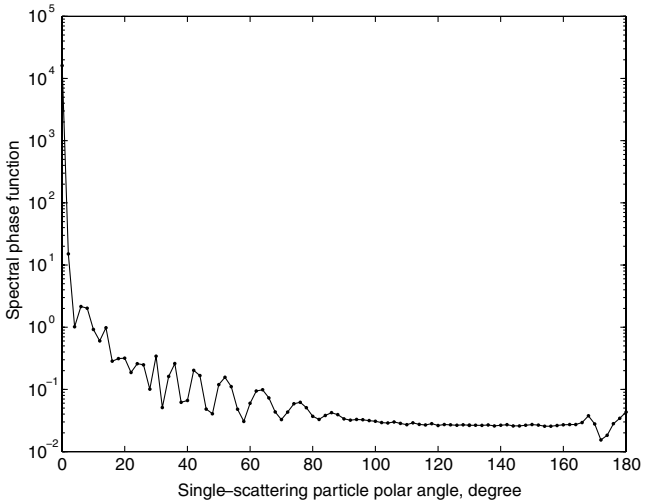

Fig. 8 Log scale spectral phase function of $D = 60$ μm at $T = 3000$ K.

$$\Phi_\lambda(\mathbf{s}\cdot\mathbf{s}') = 2f\delta(\mathbf{s}\cdot\mathbf{s}') + (1-f)\Phi^*(\mathbf{s}\cdot\mathbf{s}') \tag{28}$$

where $\Phi^*(\mathbf{s}\cdot\mathbf{s}')$ is the new approximate phase function, f is a forward-scattering fraction to be determined, and δ is the Dirac-delta function. To describe the peak in the phase function of bigger particles, f needs to be 1, meaning that $\Phi^*(\mathbf{s}\cdot\mathbf{s}')$ is not necessary to be known. Although we can add up all different sizes of particle phase functions through Eq. (27), we assumed that a 1.2 μm particle's phase function would be able to replace the complete one because of the dominant mass loading of 1.2 μm particles and their higher scattering efficiency (refer to Fig. 6). Based on this assumption, the effective gray phase function of particle dispersion, which is Eq. (27), becomes

$$\frac{\int_0^1 Q_s(r_n, T, \lambda)\Phi_\lambda(r_n, T, \lambda, \theta)\, \mathrm{d}f(\lambda T_e)}{\int_0^1 Q_s(r_n, T, \lambda)\, \mathrm{d}f(\lambda T_e)} \qquad n = 1\ (D = 1.2\ \mu\mathrm{m}) \tag{29}$$

canceling out the number density part.

The spectral phase functions of a 1.2 μm particle (refer to Fig. 7) have been averaged through Eq. (29) to evaluate the effective gray phase function of particle dispersion. Figure 9 shows one when the temperature is 3000 K. After the effective gray phase function is known, we used curve fitting to provide an analytical expression to the RTE solver instead of a set of discretized values. The reason why a curve fitting is used is because solid angle discretization, which decides the possible values of single-scattering particle polar angle θ,

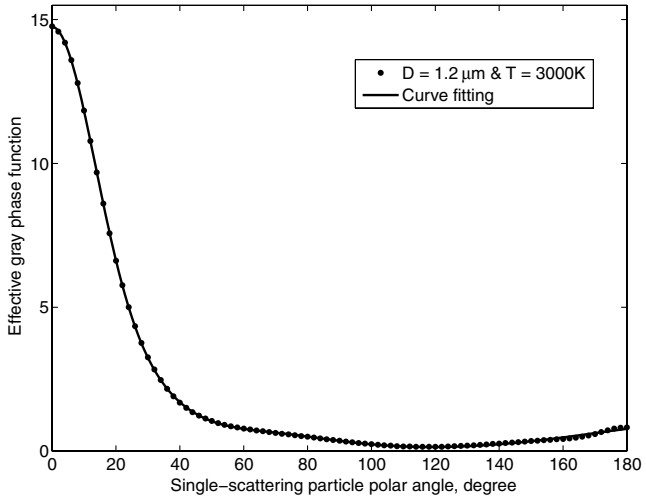

Fig. 9 Gaussian function curve fitting for the effective gray phase function.

Table 1 Coefficients for the effective gray phase function

	$i=1$	2	3	4	5	6	7	8
a_i	14	6.241	2.14	3.06	0.0	2.875	0.4159	0.4731
b_i	1.061	1.207	0.9724	1.15	0.68	−1.392	0.3982	17.5
c_i	0.05539	0.08058	0.1248	0.3894	0.001135	0.3044	0.4056	18.17

is another independent module of FVM for the RTE solver. The Gaussian function works well for this curve fitting and is shown here:

$$\Phi(\theta) = \sum_{i=1}^{8} a_i \exp\left(-\left(\frac{\theta - b_i}{c_i}\right)^2\right) \tag{30}$$

The coefficients are listed in Table 1. The same procedure is done at other temperatures and illustrated in Fig. 10.

III. Rosseland Radiation Model

The Rosseland radiation model can be used for optically thick media. The benefit of this model is that there is no need to solve the RTE to predict radiative heat flux. In a control volume, the radiative heat flux is calculated using local temperature and radiative properties. When nongray and anisotropic scattering properties are allowed for in the Rosseland radiation model, the corresponding fundamental relation for the net radiative heat flux is

$$q_r = -\frac{4}{3K_{eI,R}}\nabla e_b, \qquad e_b = \sigma T^4 \tag{31}$$

where $K_{eI,R}$ is the Rosseland mean extinction coefficient for equivalent isotropic scattering.

One of the main tasks in this work is how to define $K_{eI,R}$ in order to apply the Rosseland radiation model into a nongray full-anisotropic scattering and nonhomogeneous medium such as the internal flow in an aluminized SRM containing Al_2O_3 particles as combustion products. It is shown in [13] that Rosseland mean extinction coefficient $K_{eI,R}$ is defined as

$$\frac{1}{K_{eI,R}} = \frac{\int_0^\infty (1/K_{eI_\lambda})(\partial e_{b_\lambda}/\partial T)\,\mathrm{d}\lambda}{\int_0^\infty (\partial e_{b_\lambda}/\partial T)\,\mathrm{d}\lambda} = \int_0^1 \frac{1}{K_{eI_\lambda}}\,\mathrm{d}f_i(\lambda T) \tag{32}$$

Wavelength λ has been noted as a variable for clarification. Volumetric properties can be obtained from individual particle Mie scattering properties by adding up the effect of all the particles of different sizes and properties in a small volume. Because the particles are assumed to have the same composition but different sizes, the size distribution must be accounted for as follows:

$$K_{eI_\lambda} = \sum_{r_n} \pi r_n^2 N(r_n) Q_{eI_\lambda}(r_n) \tag{33}$$

where $Q_{eI,\lambda} = Q_{a,\lambda} + Q_{sI,\lambda}$, and $Q_{sI,\lambda}$ is the equivalent isotropic scattering efficiency, which is a spectrally varying property. It is related to the actual Mie particle-scattering efficiency as

$$Q_{sI,\lambda} = Q_{s\lambda}[1 - \omega_{o\lambda}\langle\Phi_\lambda\rangle] \tag{34}$$

where $\langle\Phi_\lambda\rangle$ is anisotropic scattering asymmetry parameter. By its definition, it includes the real anisotropic scattering behavior under an optically thick condition:

$$\begin{aligned}
\therefore \frac{1}{K_{eI,R}} &= \frac{1}{\sum_{r_n}\pi r_n^2 N(r_n)} \int_0^1 \frac{1}{Q_{eI_\lambda}(r_n)}\,\mathrm{d}f_i(\lambda T) \\
K_{eI,R} &= \frac{\sum_{r_n}\pi r_n^2 N(r_n)}{\int_0^1 (1/[Q_{eI_\lambda}(r_n)])\,\mathrm{d}f_i(\lambda T)} \\
&= \frac{\sum_{r_n}\pi r_n^2 N(r_n)}{\int_0^1 (1/[Q_{a_\lambda}(r_n) + Q_{sI_\lambda}(r_n)])\,\mathrm{d}f_i(\lambda T)} \\
&= \sum_{r_n}\pi r_n^2 N(r_n)\gamma_{\mathrm{pn}} = \lim_{V\to 0}\sum_{n=1}^{N}\frac{A_{\mathrm{pn}}}{V}\gamma_{\mathrm{pn}}
\end{aligned} \tag{35}$$

The parameter γ_{pn} may be reasonably referred to as the Rosseland mean extinction efficiency of the particles and has been defined as

$$\gamma_{pn} \Leftrightarrow \frac{1}{\int_0^1 (1/[Q_{a,\lambda}(r_n) + Q_{sI,\lambda}(r_n)])\,\mathrm{d}f_i(\lambda T)} \tag{36}$$

Equation (35) is composed of two parts: the part dependent on particle size and number density,

$$\sum_{r_n}\pi r_n^2 N(r_n)$$

and the part describing an individual particle's mean extinction efficiency, γ_{pn}. Equation (36) has been applied to the same SRM model used for the FVM, and the result is presented in Fig. 11. It shows that γ_{pn} tends to increase with temperature. For larger particles ($D = 60$–340 μm), γ_{pn} tends to increase with size as well, although size does not seem as influential as temperature. Both effects are due to the increase in extinction cross section or efficiency with

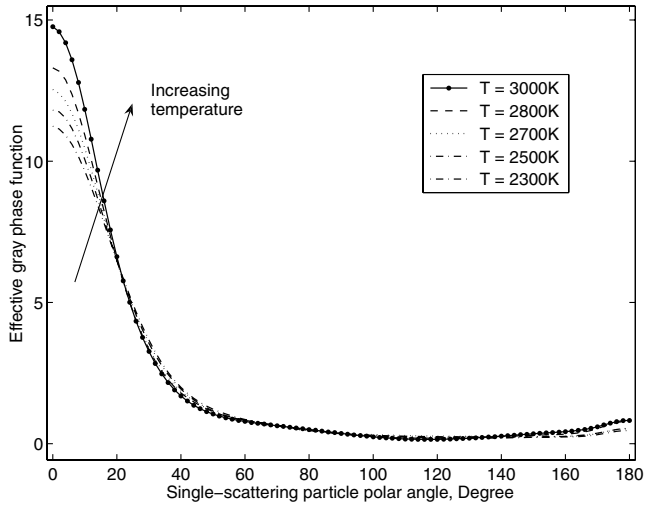

Fig. 10 Effective gray phase functions of $D = 1.2$ μm.

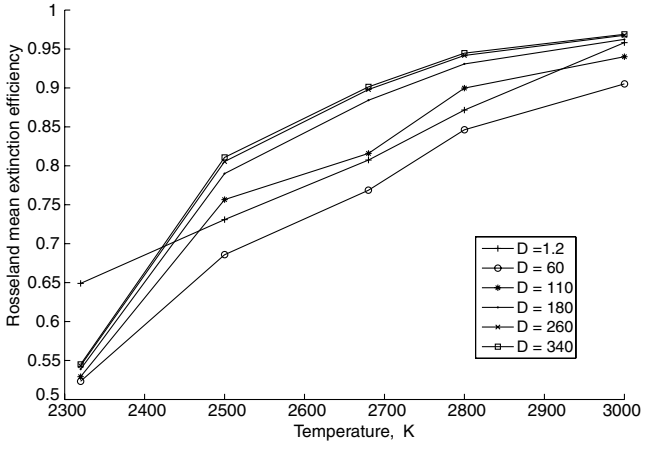

Fig. 11 Rosseland mean extinction efficiency of particles for an optically thick assembly of molten alumina particles of various diameters as a function of temperature.

increasing particle size parameter, as discussed before. For 1.2 μm particles, scattering dominates; for the larger particles, absorption dominates. Nevertheless, the sum is approximately the same for both. Thus, the extinction values for γ_{pn} are approximately the same for all particles (that is, the extinction for the 1.2 μm smoke particles is not greatly different from that of the larger particles for given temperatures). Additional data for alumina optical constants may be considered to see if these conclusions depend on the use of a particular set of optical constants from [17].

IV. Application to a Subscale SRM

So far, we have defined and evaluated effective gray radiative properties and the scattering phase function. To estimate radiative transport in an aluminized SRM, the internal flow must be simulated. This simulation was conducted with the CFD code FLUENT.

A. Aluminized SRM Internal Flow

The internal flow of an aluminized SRM can be modeled as consisting of two phases: a continuous phase and a discrete particle phase. The continuous phase consists of the gaseous combustion products of the nonmetallic propellant ingredients, which are primarily ammonium perchlorate and a binder. The discrete phase consists of condensed-phase particulate matter associated with the aluminum in the propellant. Aluminum generally burns in a somewhat distributed manner away from the propellant surface, extending possibly throughout the internal port of the motor, whereas the nonmetallic ingredients burn essentially at (within microns of) the propellant surface. Therefore, the discrete phase, in general, could include both reactant aluminum and product Al_2O_3, depending on how the distributed nature of the Al combustion was treated. In this work, aluminum is modeled under the assumption of complete combustion at the propellant surface (not distributed throughout the motor), Therefore, the discrete phase consists only of Al_2O_3. Aluminum combustion is still an area of active research, but it is known that it burns in such a manner as to form a bimodal size distribution of Al_2O_3. Submicron- or micron-size smoke particles are produced in a detached diffusion-flame envelope that surrounds each burning aluminum droplet. At the same time, there is also an accumulation of oxide on the surface of the burning aluminum droplet that forms a lobe or cap of oxide with dimensions of the same order as the aluminum droplet: namely, tens or hundreds of microns. The dominant mechanisms of oxide cap formation are still uncertain, but heterogeneous surface reaction and thermophoretic transport are thought to play a role. In any case, a bimodal size distribution of Al_2O_3 results due to these various complex combustion mechanisms. In the present model, both the micron-sized smoke particles and the larger Al_2O_3 residual cap/droplets comprise the discrete phase. Both modes of oxide are generally above the melting point of 2320 K. To simulate this two-phase flow, the Eulerian-Lagrangian approach was used. The continuous phase was computed using Eulerian analysis, whereas the motion of the discrete phase was tracked with Lagrangian description.

The steady mass-, momentum-, and energy-conservation equations for the continuous phase can be written as

$$\nabla \cdot (\rho \mathbf{v}) = 0 \tag{37}$$

$$\nabla \cdot (\rho \mathbf{v}\mathbf{v}) = -\nabla P + \nabla \cdot (\bar{\tau}) \tag{38}$$

$$\nabla \cdot (\mathbf{v}(\rho E + P)) = \nabla \cdot (\kappa \nabla T + (\bar{\tau} \cdot \mathbf{v})) + S_h \tag{39}$$

where κ is the thermal conductivity, $\bar{\tau}$ is the stress tensor, and S_h is an additional heat source by radiation. In Eq. (39), E is the total energy, given for an ideal gas by

$$E = h - \frac{P}{\rho} + \frac{v^2}{2} \tag{40}$$

where h is the sensible enthalpy.

The equation of the discrete-phase particles motion can be written as

$$\frac{\mathrm{d}\mathbf{v}_p}{\mathrm{d}t} = F_D(\mathbf{v} - \mathbf{v}_p) \tag{41}$$

where $F_D(\mathbf{v} - \mathbf{v}_p)$ is the drag force per unit particle mass and

$$F_D = \frac{18\mu}{\rho_P D^2} \frac{C_D Re}{24} \tag{42}$$

where $\mathbf{v}_P$, D, μ, and C_D are the particle velocity, diameter, molecular viscosity of the continuous phase, and drag coefficient. To simulate the dispersion of particles due to turbulence, $\mathbf{v}$ of the discrete-phase model is the instantaneous velocity of the continuous phase instead of the mean velocity. The turbulence effect is added using a renormalization-group-based κ-ε model with standard wall-function treatment. In Eq. (42), the Reynolds number is defined as

$$Re = \frac{\rho D|\mathbf{v}_P - \mathbf{v}|}{\mu} \tag{43}$$

Although the continuous phase always impacts the discrete phase, the effect of the discrete phase on the continuum can be incorporated, which is called *two-way coupling*. The momentum/heat transfer from the continuum to the discrete phase appears as a momentum/energy sink in the continuous-phase momentum/energy balance. The mechanism of the momentum/heat transfer is the drag force and the convective and radiative heat transfer, respectively. Because particles are modeled as nonreacting, there is no mass exchange. This implies that particles can be cooled or heated but noncombustible.

The boundary conditions used with the continuous phase are as follows. The head end and nozzle walls are considered to be adiabatic. At the nozzle exit, pressure is specified as 101 kPa. At the propellant surface, the flow is injected normal to the boundary, and the mass flow rate and the total temperature are set at 6.77 kg/s and 3655 K.

The injected discrete phase through the propellant surface is modeled as follows. The sizes of the injected particles are 1.2, 60, 110, 180, 260, and 340 μm, and the corresponding mass flow rates are 2.48, 0.25, 0.05, 0.15, 0.1, and 0.2 kg/s, respectively. The 1.2 μm particles simulate smoke that is produced by combustion in the detached diffusion-flame envelope already discussed. The larger particles represent a distribution of residual cap particles. As a wall boundary condition for particles, when a particle hits the head end and nozzle walls, it is recorded as trapped. If it hits the center symmetry line, it is reflected. The specific mass flow rates are from the 75 lb BATES motor test case.

Radiation is simulated with the FVM based on the discrete ordinate model. Each octant of the angular space ($4\pi/8$ sr) at any spatial location was discretized into 3×3 solid angles (3 polar and 3 azimuthal angles, respectively). At the propellant surface, the temperature is assumed to be a typical burning-surface temperature, 1000 K, and the emissivity is 0.95. For the nozzle exit, the plume effect is considered as a nonreflective opaque medium having the same temperature as the continuous-phase value at the exit plane. The walls (head end and nozzle walls) are assumed to be opaque, gray, and diffuse, with 0.9 for the emissivity.

The geometry is that of the 75 lb BATES motor at the initial grain configuration. The computational grid consists of 45 grid points distributed along the radial direction and 181 grid points distributed along the motor axis. Figure 12 shows the computational grid and boundary names.

In terms of the numerical method, the pressure-based segregated solver was used. Differencing schemes used were power law and second-order upwind schemes. The solution was considered to be converged when scaled residuals diminished as the number of iterations increased, and the average head-end pressure stopped

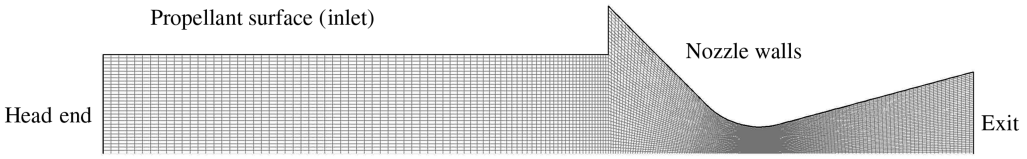

Fig. 12 Computational grid and boundary names.

changing. Specifically, the averaged head-end pressure was around 6550 kPa (950 psi), which is close to the 75 lb BATES motor's experimental data. Figure 13 shows a general convergence history of the averaged pressure on the head end.

It was observed that including radiation in the simulation affected convergence. As the internal flow solution gets close to a steady state, the pressure is supposed to approach a constant value. With radiation included (with RTE), the pressure becomes constant to within 6550 kPa after around 800 iterations, which is slower than the case without RTE. The reason the case with RTE has a noticeable oscillation and slower convergence is as follows. In both cases, the computation allows the discrete phase to interact with the continuous phase every 50 iterations. At each interaction, the particle spatial distribution changes, causing the radiative properties of the flowfield to change. This changes the radiation heat source in the energy equation, whereas such a change does not occur in the case without RTE. As the residual of the discrete ordinate model diminishes (meaning a stable radiation heat source term in the energy equation), the oscillation becomes smooth.

B. Incorporation of Particles Radiative Properties

The effective gray radiative properties (i.e., ε_{pn}, f_{pn} ρ_{pn}, and $\Phi(\mathbf{s}\cdot\mathbf{s}')$, which are the appropriate input forms for the FVM of the discrete ordinate model) have been evaluated and applied to the 75 lb BATES motor test case. Although γ_{pn} for the Rosseland radiation model has been defined and calculated, it has not been used here. This is because the current Rosseland radiation model does not have the capability to incorporate radiation by particles into the continuous phase. This work will be addressed in the future.

Figures 14 and 15 show absorption coefficient and scattering coefficient contours, respectively. Although the representative value of the absorption coefficient is 150 (1/m), it is 3000 (1/m) in the case of scattering. In general, the scattering coefficient is about a factor of 20 times larger than the absorption coefficient. This is consistent with the fact that 1.2 μm particles are highly scattering (Fig. 4) and dominant in terms of number density and surface area. A useful way to evaluate the radiative properties in the motor is through the opacity, as indicated by the mean free photon path, which is the inverse of extinction coefficient. Figure 16 shows that the typical value of the mean free photon path is about 0.3 mm. Therefore, considering the diameter of the motor (about 200 mm), the internal flow in the SRM is optically

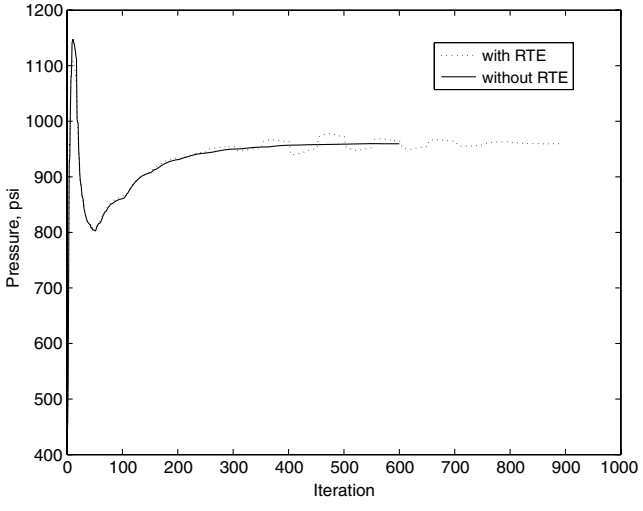

Fig. 13 Convergence history of static pressure on head end.

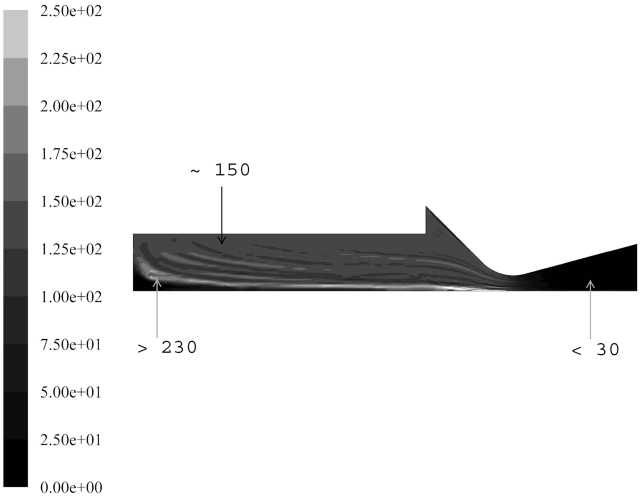

Fig. 14 Absorption coefficient by particles (1/m).

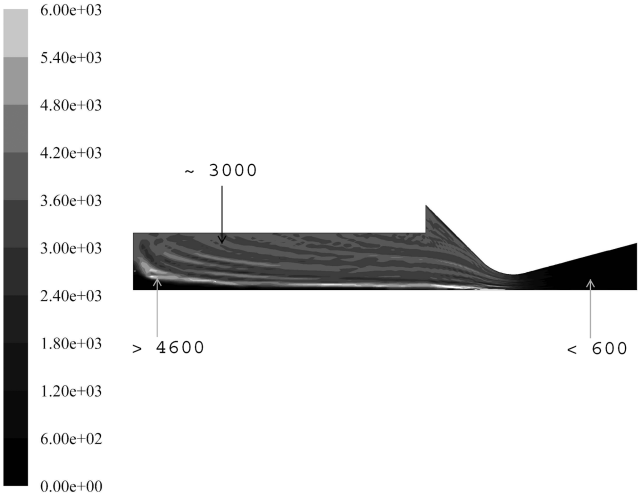

Fig. 15 Scattering coefficient by particles (1/m).

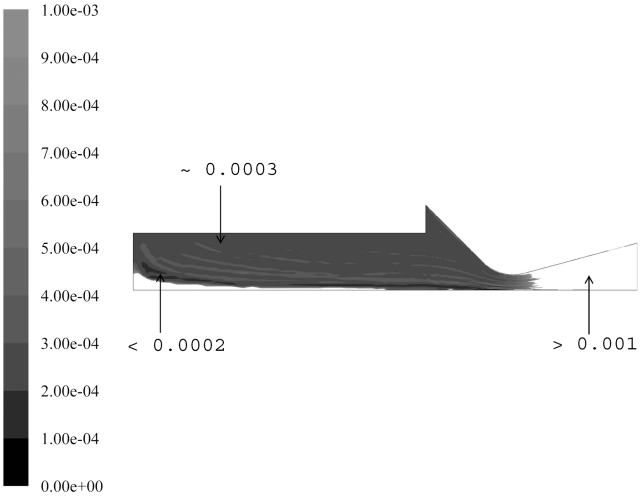

Fig. 16 Mean free photon path (in meters).

very thick. The head-end region near the symmetry (center) line is relatively optically thin because fewer particles tend to be transported into this region by the flow. It is observed that the nozzle region is also optically thin. This is caused by the following facts: First, over Mach number 1.5, there is a significantly lower concentration of particles. Second, more than half of the bigger particles ($D = 60$–320 μm) are lost to the nozzle wall (trapped) in front of the throat of the nozzle. Third, the particles in the nozzle (which are mostly $D = 1.2$ μm) have lower temperature (i.e., lower emission and scattering efficiency). The similarity in appearance, that is, spatial structuring, of Figs. 14–16 is due to the fact that all the properties (absorption, scattering, and mean free photon path) depend on the same particle number density. The spatial wiggling in the contours, especially in the chamber, is due to the fact that the particles are subject to instantaneous velocity (mean plus fluctuation) of the continuous phase instead of mean velocity only. The discrete lines in the nozzle are because the particle paths spread out in a diverging supersonic flow.

V. Conclusions

In this work, the issue of how to define radiative properties of smoke particles (molten Al_2O_3) in a solid rocket motor (SRM) was addressed in order to be compatible with existing radiative transfer equation (RTE) solvers. The individual particle's radiative properties, which are nongray and anisotropic in-scattering, were evaluated from the fundamental particle-scattering theory for spheres (i.e., Mie theory) and optical constants from literature, including temperature and spectral dependence. An integration procedure over wavelength was implemented to make use of the effective gray form of two common RTE solvers: the finite volume method and the Rosseland radiation model. The following results for effective gray radiative properties were found:

1) The individual particle emissivity/absorptivity increases as its temperature increases. The smallest particle considered (1.2 μm) has an emissivity/absorptivity roughly 10 times lower than the larger particles considered (60–340-μm) over the temperature range of 2300–3000 K. In spite of this individual characteristic, the volumetric emission/absorption in the motor is dominated by 1.2 μm particles because of their dominant mass loading (number density and surface area).

2) The smallest particle (1.2 μm) reflectivity increases as its temperature increases, whereas the larger particle (60–340-μm) reflectivity decreases. Furthermore, 1.2 μm particle reflectivity is higher than that for bigger particles over the temperature range of 2300–3000 K. For example, at 3000 K, the former is 2 times higher than the latter. Because of the higher reflectivity and mass loading of 1.2 μm particles, the scattering of the motor is also dominated by the 1.2 μm particle dispersion.

3) The effective gray phase function of the dominant 1.2 μm particles is strongly forward-scattering and becomes more so as the temperature of the particle dispersion increases.

4) The Rosseland mean extinction efficiency, which can describe a nongray and anisotropically scattering medium, has been defined and calculated for alumina smoke particles. It tends to increase with temperature as well as particle size, but the temperature is more influential.

5) In general, the scattering coefficient is about a factor of 20 times larger than the absorption coefficient. This is consistent with the fact that the spectrally averaged single-scattering albedo of 1.2 μm particles is greater than 0.95.

6) The SRM internal flow simulation, including radiative heat transfer, reveals that the scattering coefficient is about a factor of 20 times larger than the absorption coefficient and the flowfield is very optically thick, with an average photon mean free path of approximately 0.3 mm.

Acknowledgments

Support for this work from NASA and ATK-Thiokol and helpful discussion with Jim Braithwaite, Andy Eaton, and Steve Cannon are gratefully acknowledged.

References

[1] Brewster, M. Q., and Parry, D. L., "Radiative Heat Feedback in Aluminized Solid Propellant Combustion," *Journal of Thermophysics and Heat Transfer*, Vol. 2, No. 2, 1988, pp. 123–130. doi:10.2514/3.75

[2] Ishihara, A., Brewster, M. Q., Sheridan, T. A., and Krier, H., "The Influence of Radiative Heat Feedback on Burning Rate in Aluminized Propellants," *Combustion and Flame*, Vol. 84, Nos. 1–2, 1991, pp. 141–153. doi:10.1016/0010-2180(91)90043-B

[3] Tang, K. C., and Brewster, M. Q., "Numerical Analysis of Radiative Heat Transfer in an Aluminum Distributed Combustion Region," *Numerical Heat Transfer, Part A, Applications*, Vol. 22, No. 3, 1992, pp. 323–342. doi:10.1080/10407789208944771

[4] Cho, I. H., Baek, S. W., and Chang, S. T., "A Numerical Simulation of Axisymmetric Solid Rocket Motor Ignition Transient with Radiation Effect," AIAA Paper 96-2906, July 1996.

[5] Jung, H. G., Lee, C., and Lee, J. W., "Role of Radiation on Dynamic Extinction by Depressurization in Metallized Solid Propellants," *Journal of Propulsion and Power*, Vol. 20, No. 3, 2004, pp. 432–439. doi:10.2514/1.10384

[6] Duval, R., Soufiani, A., and Taine, J., "Coupled Radiation and Turbulent Multiphase Flow in an Aluminised Solid Propellant Rocket Engine," *Journal of Quantitative Spectroscopy and Radiative Transfer*, Vol. 84, No. 4, 2004, pp. 513–526. doi:10.1016/S0022-4073(03)00268-1

[7] Raithby, G. D., and Chui, E. H., "A Finite-Volume Method for Predicting a Radiant Heat Transfer in Enclosures with Participating Media," *Journal of Heat Transfer*, Vol. 112, No. 2, 1990, pp. 415–423. doi:10.1115/1.2910394

[8] Chai, J. C., Lee, H. S., and Patankar, S. V., "Finite-Volume Method for Radiation Heat Transfer," *Journal of Thermophysics and Heat Transfer*, Vol. 8, No. 3, 1994, pp. 419–425. doi:10.2514/3.559

[9] Murthy, J. Y., and Mathur, S. R., "Finite-Volume Method for Radiative Heat Transfer Using Unstructured Meshes," *Journal of Thermophysics and Heat Transfer*, Vol. 12, No. 3, 1998, pp. 313–321.

[10] Sabnis, J. S., "Numerical Simulation of Distributed Combustion in Solid Rocket Motors with Metallized Propellant," *Journal of Propulsion and Power*, Vol. 19, No. 1, 2003, pp. 48–55.

[11] Ahmad, R. A., "Internal Flow Simulation of Enhanced Performance Solid Rocket Booster for the Space Transportation System," AIAA Paper 2001-3585, July 2001.

[12] Geisler, R. L., Kinkead, S. A., and Beckman, C. W., "The Relationship Between Solid Propellant Formulation Variables and Motor Performance," AIAA Paper 75-1199, September 1975.

[13] Brewster, M. Q., *Thermal Radiative Transfer and Properties*, Wiley Interscience, New York, 1992.

[14] "FLUENT 6.2 User's Guide," Fluent, Inc., Lebanon, NH, Jan. 2005.

[15] Lockwood, F. C., Rizvi, S. M. A., and Shah, N. G., "Comparative Predictive Experience of Coal Firing," *Proceedings of the Institution of Mechanical Engineers Part C, Mechanical Engineering Science*, Vol. 200, 1986, pp. 79–87.

[16] Modest, M. F., *Radiative Heat Transfer*, McGraw–Hill, New York, 1993.

[17] Parry, D. L., and Brewster, M. Q., "Optical Constants of Smoke in Propellant Flames," *Journal of Thermophysics and Heat Transfer*, Vol. 5, No. 2, Apr.–June 1991, pp. 142–149. doi:10.2514/3.241

[18] Gal, G., and Kirch, H., "Particulate Optical Properties in Rocket Plumes," U.S. Air Force Rocket Propulsion Lab., TR-73-99, Edwards AFB, CA, Nov. 1973, pp. 180–197.

[19] Mularz, E. J., and Yuen, M. C., "An Experimental Investigation of Radiative Properties of Aluminum Oxide Particles," *Journal of Quantitative Spectroscopy and Radiative Transfer*, Vol. 12, No. 11, 1972, pp. 1553–1568. doi:10.1016/0022-4073(72)90130-6

T. Lin
Associate Editor